

See discussions, stats, and author profiles for this publication at: <https://www.researchgate.net/publication/262577334>

Effect of Precursor Stoichiometry on the Morphology of Nanoporous Platinum Sponges

ARTICLE in ACS APPLIED MATERIALS & INTERFACES · MAY 2014

Impact Factor: 6.72 · DOI: 10.1021/am501794y · Source: PubMed

CITATIONS

8

READS

36

5 AUTHORS, INCLUDING:



Supitcha Supansomboon

Srinakharinwirot University

10 PUBLICATIONS 50 CITATIONS

SEE PROFILE



Alexander Porkovich

5 PUBLICATIONS 16 CITATIONS

SEE PROFILE



Annette Dowd

University of Technology Sydney

49 PUBLICATIONS 314 CITATIONS

SEE PROFILE



Michael B Cortie

University of Technology Sydney

216 PUBLICATIONS 3,827 CITATIONS

SEE PROFILE

Effect of Precursor Stoichiometry on the Morphology of Nanoporous Platinum Sponges

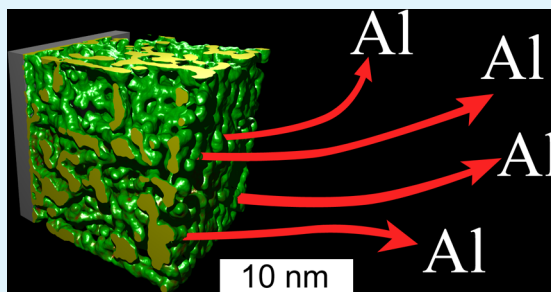
Supitcha Supansomboon, Alexander Porkovich, Annette Dowd, Matthew D. Arnold, and Michael B. Cortie*

Institute for Nanoscale Technology, University of Technology Sydney, PO Box 123, Broadway, NSW 2007, Australia

S Supporting Information

ABSTRACT: Nanoscale sponges formed by de-alloying suitable metallic alloys have a wide variety of potential applications due to their enhanced catalytic, optical, and electrochemical properties. In general, these materials have a bi-continuous, vermicular morphology of pores and ligaments with a *fibrous* appearance; however, other morphologies are sometimes reported. Here, we investigate how stoichiometry and process parameters control the characteristics of sponges formed from thin film precursors of Al_xPt . Materials deposited at elevated temperatures and with mole fraction of Al between 0.65 and 0.90 produce the classic isotropic *fibrous* sponges with a morphology that varies systematically with precursor stoichiometry; however, de-alloying of material deposited at room temperature produced unusual isotropic *foamy* sponges. The evidence suggests that formation of a conventional fibrous sponge requires an equilibrated precursor whereas foamy morphologies will result if the precursor is metastable. Modeling was used to investigate the range of possible morphologies. As stoichiometry changed in the model system, the average mean and Gaussian curvature of the sponges systematically changed, too. The evolution of these shapes passed through certain special morphologies; for example, modelled structures with 0.80 Al had a zero average Gaussian curvature and might represent a structural optimum for some applications. These observations provide a means to control sponge morphology at the nanoscale.

KEYWORDS: nanoporous sponge, platinum, de-alloying, curvature, Monte Carlo model



INTRODUCTION

De-alloying of alloys formed between noble and active metals can produce nanoscale metallic sponges with a bi-continuous, bi-vermicular network of metal ligaments and open channels.¹ These structures have a geometric affinity to those produced by a spinodal decomposition.^{2,3} In the prototypical case, the solid ligaments and open channels of this type of sponge are topologically and morphologically equivalent.⁴ There is, however, a less-commonly reported sponge morphology: an isotropic foam created by interconnected spherical cavities.^{5–7} To avoid confusion between these two types of sponge, we suggest that the former be termed an isotropic fibrous sponge, and the latter an isotropic foam sponge. In addition, other morphologies, such as the ‘cracked mud’ sponge formed by shrinkage and fracture of a de-alloyed matrix^{8,9} or anisotropic fibrous sponges with metal ligaments aligned in the growth direction,^{5,10} have also been reported.

The reduction potential of the active element (Al in our case) must be considerably less than that of the noble element in order for sponge formation to occur. The greater the difference between the two potentials, the greater the tendency towards de-alloying.¹¹ The noble element in these sponges can be Au, Pt, Ag, Pd, or Cu while the active element may be Al, Mg, Sn, or Si (however, Cu or Ag may serve as the active element if alloyed with an even more noble element such as Au

or Pt).^{7,8,12–17} In addition, the mole fraction, χ_{Al} , of the active element must be at least greater than about 0.5 (the ‘parting limit’ or de-alloying threshold).^{11,18,19} A χ_{Al} in the range from about 0.65 to 0.88 is considered most suitable for formation of fibrous sponges, both generally^{2,8,13,14,17,20} and for Al_xPt specifically.^{7,21,22} However, there has been little attention paid to the several other sponge morphologies that are possible. In the present paper, we investigate this by systematically varying χ_{Al} from 0.50 to 0.98 and investigating the effect of heat-treatment on the precursor alloy. We find that there is a surprising diversity of sponge morphologies and, importantly, some clear principles that control their formation.

It is pertinent that the Al–Pt binary system is relatively complex with a number of intermetallic compounds²³ and some uncertainty regarding individual phases.^{23,24} *Inter alia*, a previously-reported^{24–27} cubic $\text{Al}_{21}\text{Pt}_5$ has been most recently established to be trigonal Al_4Pt (with stoichiometry $\text{Al}_{21}\text{Pt}_{5.3}$),²⁸ while metastable compounds Al_6Pt , Al_5Pt (‘ ϵ -phase’), Al_4Pt , $\text{Al}_{21}\text{Pt}_6$, and Al_3Pt have also been reported.^{23,27,29–31} The existence of Al_2Pt and $\text{Al}_{21}\text{Pt}_8$ is not controversial.^{23–26}

Received: March 25, 2014

Accepted: May 22, 2014

Published: May 22, 2014



In the present work, we prepared thin films of Al_xPt by co-depositing the elements using magnetron sputtering, followed by de-alloying of the Al in NaOH solution. To gain further insight, we also modeled the de-alloying process using a hybrid of Monte Carlo and cellular automaton algorithms. In this toy physics model, lowly coordinated atoms of an active metal (designated A) are removed from surface sites of a solid solution with a noble metal (designated N) by a 3D cellular automaton while, simultaneously, an off-lattice Metropolis Monte Carlo routine using the Lennard-Jones potential thermally anneals the remaining atoms. The simulated sponge structures were observed to closely resemble the experimental ones, a point which we analyze and explore.

■ EXPERIMENTAL PROCEDURE

Synthesis. All samples were prepared by co-depositing the elements onto inert substrates (glass, silicon, or austenitic stainless steel foil) by direct current magnetron sputtering. Substrate surfaces had been previously cleaned using detergent, water, and/or acetone then dried in N_2 . The temperature of the substrate could be controlled between ambient and a nominal 400 °C during the deposition. The base pressure of the chamber was 1.3×10^{-4} Pa ($\sim 10^{-6}$ Torr), and there was a flow of Ar at a pressure of 0.27 Pa (2 mTorr) during deposition. The composition of the deposits was controlled by varying the current or power applied to the individual targets and by monitoring deposition rates on a quartz crystal sensor. Sample composition was verified afterwards by X-ray diffraction and by EDS analysis on a SEM. A series of Al–Pt samples, with Al contents varying from 0 at. % to ~ 95 at% were prepared. The pure Pt sample was used as a comparator for the X-ray diffraction studies. De-alloying of selected samples was achieved by immersing samples in either an aqueous solution of 0.2 M NaOH, a process which took two to 3 min, or in a 1M solution of Na_2CO_3 , a process that took several minutes. The process was assumed to be complete once no further bubbles of H_2 were evolved.

Characterization. Samples were characterized by X-ray diffraction on (1) a Siemens D5000 Diffractometer using $\text{Cu K}\alpha$ radiation ($\lambda = 0.15406$ nm at a tilt angle of 0.5°), (2) on the powder diffraction beamline at the Australian Synchrotron using a standard flat plate arrangement inside an Anton Paar furnace with an argon atmosphere ($\lambda = 0.1261$ nm, incident angle Ω of 2° and beam cross-section $4 \text{ mm} \times 0.2 \text{ mm}$), and (3) at the Australian Synchrotron on custom-made flat plate arrangement ($\lambda = 0.1378$ nm and incident angle 0.3°). Relatively low energy beams were used at the synchrotron in order to minimize contributions from the substrate. Wavelength was calibrated using LaB_6 and diamond standards. Scanning electron microscopy and electron dispersive analysis of the compositions was conducted on a Zeiss Supra 55VP SEM. Charging of some of the porous platinum deposits was a problem in some instances, indicating poor percolation. Transmission electron microscopy was carried out on selected de-alloyed samples using a 200 kV JEOL 2200FS or a 20 kV Philips CM12. The fragments of spongy de-alloyed material were collected on holey carbon coated copper TEM grids and imaged without further preparation.

Numerical Simulation. Simulation of the de-alloying of the sponges was carried out using a code composed of a Metropolis Monte Carlo algorithm (to move atoms into lowest energy positions) and a stochastic cellular automaton which removed any lowly-coordinated Al atoms. The simulations were generally carried out on cubes of 119 000 starting atoms to generate quantitative data on morphology, but a cube of 900 000 atoms was used to generate images of isotropic foams. The unit of time in these simulations is a ‘sweep’, with one sweep defined as the number of iterations of the simulation that on average would result in each ‘atom’ being visited once. The ‘atoms’ were arranged either in a random fcc solid solution of Al and Pt, or in a duplex microstructure consisting of a matrix of (Al,Pt) solid solution and spherical precipitates of Al. The model is a real-space simulation with atoms located on non-integer spatial coordinates. Such

a problem normally scales in time as $O(n^3)$ and would normally be intractable for a million atoms. In the present instance, reasonable computational efficiency was achieved by hashing all atomic coordinates to a 3D hash array, while further acceleration was achieved by directing the simulation to operate in the vicinity of free surfaces only. The code was written in Pascal and is available on request in Lazarus format for use on a variety of platforms.

Analysis of Simulated Morphology. The average mean, $\langle M \rangle$, and Gaussian, $\langle G \rangle$, curvatures of surface regions of the simulated sponges were computed by fitting biquadratic surface patches with a diameter of about 3.0 Lennard-Jones (LJ) length units to 5000 randomly chosen locations on the surface of each sponges and averaging the results. The surface-fitting algorithm was run against calibration surfaces to verify its accuracy. The technique proved usable for mean curvatures between about -0.50 and $+0.34$ reciprocal LJ length units, corresponding approximately to physical curvatures in the range -0.25 to $+0.35 \text{ nm}^{-1}$. The scheme is less reliable for greater curvatures (smaller radii) because a biquadratic patch cannot be readily fitted to acutely curved regions. Fortunately, the sponges in the present simulations generally possessed smooth surfaces, with curvatures well within the range of the numerical technique, because of the strong tendency of surface tension to remove asperities. The same code calculated the ratio, ν , of surface atoms to total atoms.

■ RESULTS AND DISCUSSION

Two important factors were established early in the work. First, the microstructures of precursor films deposited at 300 °C or greater were crystalline, with the phases present controlled by the stoichiometry, whereas those deposited at room temperature had weakly developed diffraction patterns indicating that were nearly amorphous. Secondly, precursors with $\chi_{\text{Al}} < 0.60$ did not form sponges under our experimental de-alloying conditions (i.e. were below the parting limit) so will not be discussed further here.

According to the phase diagram, precursors with $0.60 < \chi_{\text{Al}} < 0.67$ should have been 100% Al_3Pt_2 at $\chi_{\text{Al}} = 0.60$ and 100% Al_2Pt at $\chi_{\text{Al}} = 0.67$, with a duplex microstructure at intermediate stoichiometries. In the case of samples deposited at *elevated temperature* this was confirmed by XRD and visual examination, with the cubic diffraction pattern and characteristic brassy yellow color³² of Al_2Pt becoming more prominent as χ_{Al} approached 0.67. However, it was found to be essential to retard oxidation of Al during sample manufacture otherwise Al_3Pt_2 formed at the expense of Al_2Pt . In contrast, samples deposited at room temperature were not crystalline until heat treated to in excess of 400 °C. Samples with composition closer to $\chi_{\text{Al}} = 0.60$ produced partially de-alloyed ‘pinhole’ sponges (Supporting Information, Figure S1). Crystalline samples with close to the Al_2Pt stoichiometry de-alloyed rapidly to produce a porous and cracked film, with a characteristic microstructure of elongated voids, channels and cracks, surrounded by higher density material, Figure 1a. It is evident that considerable shrinkage took place, as also reported in the production of Raney-type catalysts.¹⁹ TEM revealed that the remaining Pt also contained internal spherical or vermicular porosity. The crystallinity of the material had an effect on the nature of the sponge produced. In Figure 1b, we compare the X-ray diffraction patterns of two samples with $\chi_{\text{Al}} = 0.67$, but deposited at 200 or 400 °C, and in Figure 1c the diffraction patterns of the corresponding nanoporous Pt films. It is clear that barely any crystallization of the Al_2Pt precursor occurred when the deposit was made at 200 °C and that the peaks of the porous Pt made from the nearly amorphous precursor were significantly broader than those made from the well-crystallized precursor.

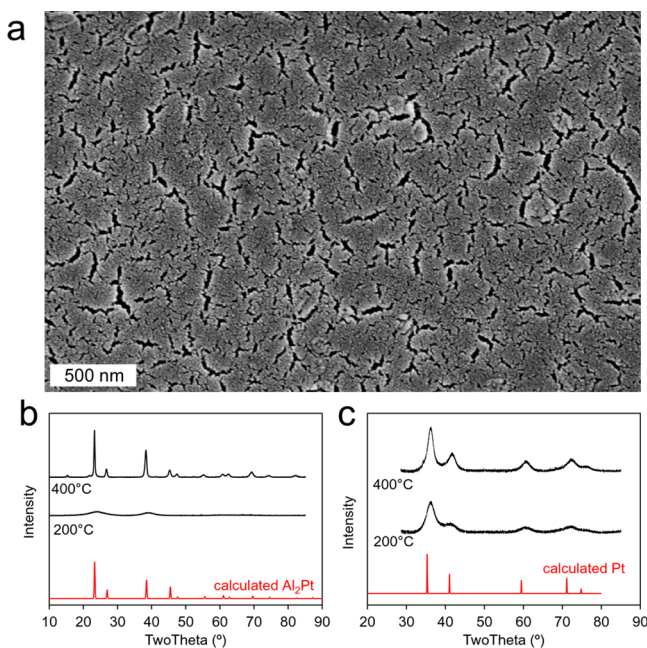


Figure 1. 'Mud-cracked' mesoporous sponges produced by de-alloying samples with $0.60 < \chi_{\text{Al}} < 0.67$. (a) SEM image of sample with $\chi_{\text{Al}} = 0.64$. (b) X-ray diffraction patterns ($\lambda = 0.1378$ nm) of the Al_2Pt precursor deposited at 200 and 400 °C showing the effect of deposition temperature. (c) X-ray diffraction pattern of porous Pt sponges produced from the corresponding samples in part b. (Precursor films are between 180 and 220 nm thick, substrate is glass.)

We next examined sponges formed from precursors in the range $0.67 < \chi_{\text{Al}} < 0.80$. According to the equilibrium phase diagram, the deposited material should have consisted of a two-phase mixture of Al_2Pt and $\text{Al}_{21}\text{Pt}_8$ for $0.67 < \chi_{\text{Al}} < 0.72$, close to 100% $\text{Al}_{21}\text{Pt}_8$ at about $\chi_{\text{Al}} = 0.73$, a mixture of $\text{Al}_{21}\text{Pt}_8$ and Al_4Pt for $0.73 < \chi_{\text{Al}} < 0.80$, and 100% Al_4Pt at about $\chi_{\text{Al}} = 0.80$. However, the situation is complicated by the possible formation of at least one (if not more) of the metastable intermetallic compounds mentioned earlier. The XRD patterns of the precursors deposited at elevated temperature were well-formed but complex, Figure 2a. It is clear that the peaks marked '*' in the samples deposited at elevated temperature could be due to the presence of metastable ϵ -phase (nominally Al_5Pt)³³ and the peaks marked 'V' in the sample made at room temperature and then annealed are probably due to the presence of some $\text{Al}_{21}\text{Pt}_8$. Samples deposited at room temperature were practically amorphous but crystallized when heated. For example, a sample with $\chi_{\text{Al}} = 0.75$, heated in a synchrotron X-ray diffraction experiment at $3^\circ\text{C}\cdot\text{min}^{-1}$, crystallized suddenly at about 360°C , Figure 2b, to form a phase with peaks that were very similar to those reported for ϵ . De-alloying of samples with $0.67 < \chi_{\text{Al}} < 0.80$ that had been deposited at elevated temperature produced classic isotropic fibrous sponges, Figure 2c. In some cases the porous Pt peeled off the substrate, which provided a convenient cross-sectional view, Figure 2d. However, the sponges produced from samples in the range $0.67 < \chi_{\text{Al}} < 0.80$ that had been deposited at room temperature were of a nature intermediate between pinhole and foamy, Figure 2d, e.

Finally, we considered the nature of the sponges formed when $\chi_{\text{Al}} > 0.80$. The microstructure should contain Al in equilibrium with Al_4Pt (the latter being ostensibly the most stable intermetallic phase in this region of the phase diagram).²⁸ The presence of Al was confirmed by XRD in samples

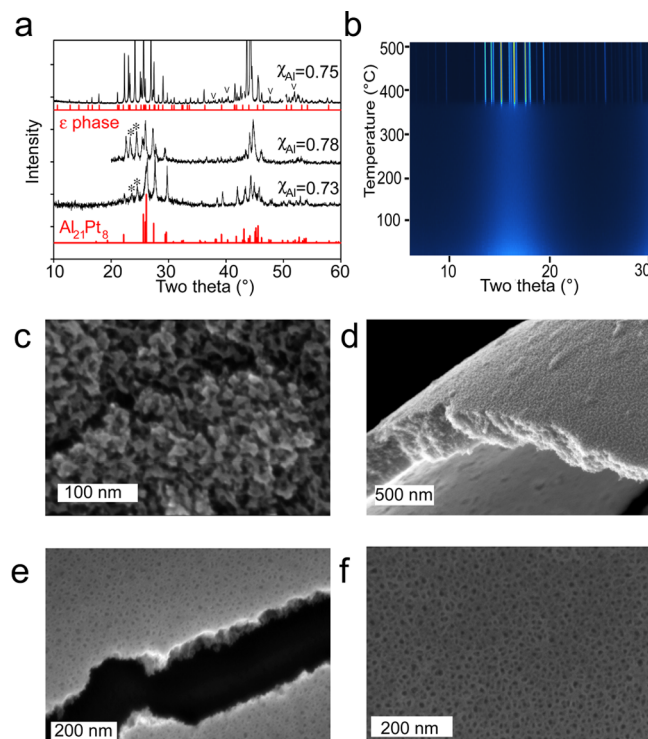


Figure 2. 'Fibrous' and 'foamy' mesoporous sponges produced by de-alloying samples with $0.67 < \chi_{\text{Al}} < 0.80$. (a) X-ray diffraction pattern of crystalline samples of $\chi_{\text{Al}} \approx 0.75$. The lattice parameter of the ϵ -phase has been inflated from the original $a = 1.358$, $c = 1.664$ nm, to $a = 1.376$, $c = 1.660$ nm to fit. Peaks marked '*' occur in ϵ but not in $\text{Al}_{21}\text{Pt}_8$ (JCPDF card 00-039-1287) and vice versa for the peaks marked 'V'. The samples marked $\chi_{\text{Al}} = 0.73$ and 0.78 were deposited at a nominal 400°C and were measured at room temperature. The sample designated $\chi_{\text{Al}} = 0.75$ was deposited at room temperature then crystallized by heating to $\sim 400^\circ\text{C}$, with its XRD pattern taken at that temperature (all 2θ are as for a λ of 0.11261 nm). (b) Crystallization of ϵ phase at $\sim 360^\circ\text{C}$ on heating up of an amorphous precursor ($\chi_{\text{Al}} = 0.75$). (c and d) Isotropic fibrous sponge produced by de-alloying sample with $\chi_{\text{Al}} = 0.74$ that had been deposited at a nominal 400°C . (e and f) Isotropic foamy sponges produced by de-alloying sample with $\chi_{\text{Al}} = 0.77$ that had been deposited at room temperature (brightness and contrast have been enhanced in these images). (Precursor films are ~ 300 nm thick. Substrate is a glass slide for all samples.)

deposited at 400°C and in samples that had been deposited at room temperature and then heated above 300°C . The height of the peaks associated with Al increased as the Al content was increased, Figure 3a. However, the most obvious other phase in these samples was ϵ , not Al_4Pt . Additionally, it was noted in the synchrotron experiments that, while Al_4Pt and ϵ precipitated more-or-less simultaneously at 335°C when the samples were heated at $3^\circ\text{C}\cdot\text{min}^{-1}$, ϵ formed before Al_4Pt in samples heated at $\sim 400^\circ\text{C}\cdot\text{min}^{-1}$. At 480°C the ϵ in both samples disappeared and only Al_4Pt was present up to 600°C . The rate of formation of the Al_4Pt was evidently related to the nature of the post-deposition heat treatment. Samples with $\chi_{\text{Al}} > 0.88$ that were heated at $\sim 25^\circ\text{C}\cdot\text{min}^{-1}$ to 460°C did not form Al_4Pt but instead crystallized to a mixture of ϵ and Al phase. Presumably further annealing or a higher temperature would have converted the ϵ in these samples to Al_4Pt . The metastable nature of the ϵ was confirmed by heating an as-deposited sample with $\chi_{\text{Al}} = 0.88$ through the series of phase transformations to 550°C to form the Al_4Pt phase and then cooling it below 480°C again to see if ϵ would reform. Since

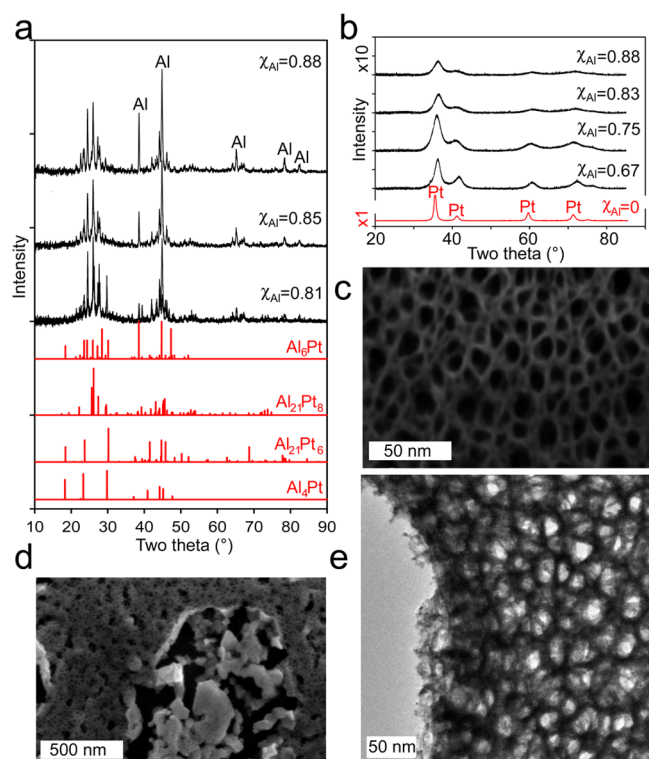


Figure 3. Effect of Al content on structure of sponges produced from precursors with $\chi_{\text{Al}} > 0.80$. (a) X-ray diffraction spectra of samples with $\chi_{\text{Al}} > 0.81$ made by depositing at a nominal temperature of $\sim 400^\circ\text{C}$. The increasing amount of elemental Al as χ_{Al} increases from bottom to top is clear (2θ scale aligned with Cu K α). (b) X-ray diffraction patterns of a series of de-alloyed Pt sponges compared to that of a conventional sputtered Pt film. The decrease in crystallinity of the Pt as χ_{Al} increases is evident. The X-ray intensities of the de-alloyed films are shown at approximately 10 \times the vertical scale of the sputtered elemental Pt film ($\lambda = 0.1378$ nm here). (c) SEM micrograph of isotropic foamy Pt sponge with a bimodal distribution of pore sizes. Precursor had $\chi_{\text{Al}} = 0.88$. (d) Foamy sponges formed from a heterogeneous starting microstructure with $\chi_{\text{Al}} = 0.85$. (e) TEM micrograph of sponge formed from precursor with $\chi_{\text{Al}} = 0.88$. (Precursor films are 100 nm thick for parts c and e and 220 nm for part d. Substrate is glass in all cases.)

the sample did not revert to ε when cooled it is clear that, at $\chi_{\text{Al}} = 0.88$ at least, ε is metastable relative to Al_4Pt . Clearly, the relative proportions of ε and Al_4Pt in these samples depends closely on their thermal history. The application of X-ray diffraction to the de-alloyed samples revealed that crystallinity of the sponges systematically decreased as χ_{Al} was increased towards 0.88, Figure 3b. De-alloying of the samples deposited at room temperature produced isotropic foams, Figure 3c–e. The TEM image in particular shows that the Pt is in the form of a continuous and low density filamentaceous network that surrounds the voids. Clearly, this morphology simultaneously maximizes both percolation of the Pt and exposed surface area. As such, it may be a useful microstructure for catalytic applications. Bimodal distributions of pore sizes were possible for $0.75 < \chi_{\text{Al}} < 0.88$, for example, Figure 3d and Supporting Information Figure S2, with the different pore morphologies evidently corresponding to regions (or phases) of differing Al content in the precursor film. For example, the discontinuous phase formed in samples in which $0.66 < \chi_{\text{Al}} < 0.81$ clearly had a higher Al content than the continuous phase. Furthermore, such regions of discontinuous phase de-alloyed to form a

barely-percolating sponge which charged up noticeably more in the SEM than sponge formed from the matrix phase.

Samples with $\chi_{\text{Al}} > 0.90$ were rapidly de-alloyed and the Pt component formed a disordered and fragile mass (Supporting Information, Figure S3) that is qualitatively similar to the metallic aerogels recently reported by Herrman et al.³⁴ EDS on the TEM showed that the χ_{Al} was of the order of 0.10 to 0.15, in agreement with values in the literature.^{13,22} Evidently de-alloying with an alkali does not completely remove Al because the last vestiges of it are encapsulated by Pt.

We turned next to modeling to elucidate the sponge-forming process. As expected, this showed that sponge formation was strongly controlled by the stoichiometry of the precursor. When our model was applied to a homogenous, crystalline solid solution, the resulting morphologies varied from pinhole sponges ($\chi_{\text{Al}} \approx 0.6$) to isotropic fibrous sponges ($\chi_{\text{Al}} \approx 0.7$ to 0.8) to non-percolating nanoparticles ($\chi_{\text{Al}} > 0.9$), Figure 4a.

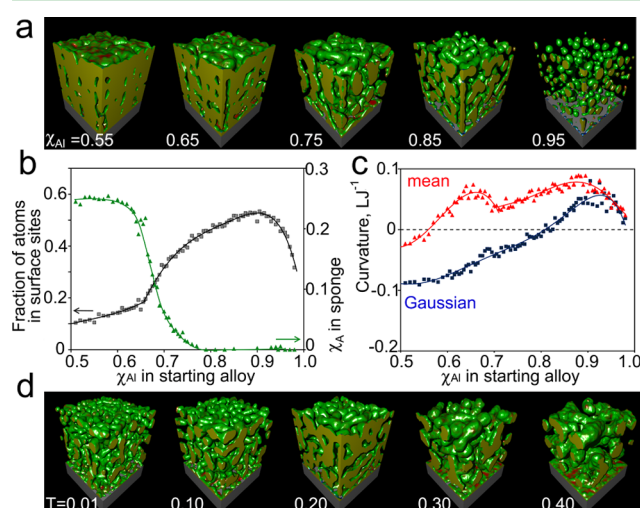


Figure 4. Morphology and properties of sponges produced by the Monte Carlo model as a function of χ_{Al} at 5000 sweeps. (a) Morphologies of sponges produced from homogenous solid solutions of 120 000 atoms, varying from pin-hole sponge to non-contiguous nanoparticles. (b) Ratio of surface atoms to total atoms of sponges (v) and χ_{Al} remaining in sponge. (c) Average mean and Gaussian curvatures of sponges. (d) Effect of Lennard-Jones temperature on the de-alloying of a starting alloy with $\chi_{\text{Al}} = 0.80$.

The simulated morphologies closely resembled those of experimental samples produced by de-alloying homogenous, crystalline samples in this and prior work.^{2,4,21,35} Furthermore, the de-alloying below a residual Al content of about χ_{Al} of 0.1 was slow, as in the real samples. Therefore, we considered that it would be useful to exploit this similarity to systematically investigate the morphology of the simulated sponges as a function of composition and de-alloying parameters. Trends in the ratio of surface to total atoms (v), average mean, $\langle M \rangle$ and average Gaussian, $\langle G \rangle$, curvatures, Figure 4b and c, and the proportions of positive or negative mean and Gaussian curvatures (Supporting Information Figure S4) were established. We also investigated the effect of increasing the simulation temperature on the morphology and found that it led to coarser sponges, as reported in the literature for real sponges,^{14,36–39} Figure 4d. The sponges become coarser because rates of both volume and surface diffusion in the Monte Carlo simulation increase with temperature, which accelerates the attainment of lower surface-to-volume ratios.

Sponges produced with $T < 0.15$ contained a larger proportion of negative curvature. The optimum range for fibrous sponges ($\langle M \rangle > 0$, $\langle G \rangle \approx 0$) was $0.15 < T < 0.25$. We suggest that, as the model sponges share obvious geometric affinities with experimental fibrous ones, the trends observed in the model sponges may be broadly applicable to the real fibrous sponges, too. In particular, there is a noticeable change in the morphologies of the sponges at $\chi_A \approx 0.67$. In the real sponges, this is the point at which a recognizably porous sample is produced, while in the simulated samples this value of χ_A is associated with a marked increase in ν and decrease in $\langle M \rangle$. Note that this transition is not correlated with the loss of site or bond percolation of the noble element atoms since, on an fcc lattice, that threshold only occurs at $\chi_A = 0.80$.⁴⁰

The mismatch between the χ_A value at the onset of de-alloying and that of the bond percolation threshold has been noted by Sieradzki¹⁸ who proposed that the explanation lay in the important role of surface diffusion. Furthermore, variation with temperature could be explained in part as due to the changing roles of volume and surface diffusion processes. Specifically, the threshold χ_A for de-alloying should rise at first in a thermally activated manner as temperature increases. This is because an increase in rate of surface diffusion will speed the formation of a passivating layer of noble metal atoms on the surface. So, at lower temperatures, an increase in temperature is expected to retard de-alloying. However, the rate of volume diffusion will also be increasing. Diffusion within the bulk of the sponge brings a replenishing supply of element A to the surface which will tend to promote sponge formation. Therefore, at some point the effect due to volume diffusion overwhelms that due to surface diffusion, and further increase in temperature decreases the χ_A threshold for de-alloying. This behavior is replicated by our model, Figure 5.

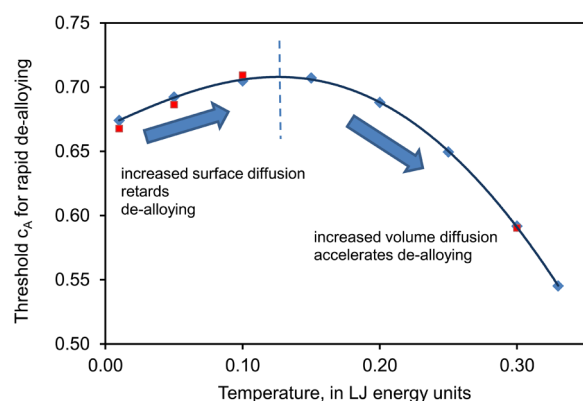


Figure 5. Effect of temperature on the de-alloying threshold, with the latter defined as the starting χ_A for which only 10% A remained after 1000 sweeps of the simulation. There is a transition from a regime controlled by surface diffusion to one controlled by volume diffusion at $T \approx 0.15$ energy units. The red symbols indicate simulations in which a vacancy concentration of 0.01 has been inserted.

In order to form a contiguous Pt solid for χ_{Al} greater than about 0.8, significant, longer range movement of the non-percolating Pt atoms must necessarily occur, but below that value of χ_{Al} only short range displacements of Pt are required or indeed even possible. It follows, therefore, that for $\chi_A < 0.8$ the residual N may inherit the grain structure of the precursor from which it was formed and indeed this has been experimentally verified when de-alloying the Au–Al alloys with $\chi_{Al} \approx 0.65$.⁴¹

However, for $\chi_A > 0.8$, this becomes less likely and instead a recrystallization of the noble metal atoms into new nanoscale crystallites will occur. These changes result in the observed systematic decrease in crystallinity of the Pt sponge as χ_{Al} is increased.

As mentioned, the modeling process produced isotropic fibrous sponges from *homogenous* crystalline precursors. This raised the questions of why foamy sponges were produced from the nearly amorphous precursors deposited at room temperature and how they might be reproduced using the model. The literature suggests that a homogenous starting solid solution is an essential prerequisite to forming fibrous nanoporous sponges.^{22,42,43} However, as shown earlier, precursors deposited at room temperature were in a metastable state and they would almost certainly be under state of biaxial tensile stress, too.⁴⁴ We speculated that, due to the nature of the Al–Pt binary phase diagram and the stochastic nature of the deposition process, they might contain nanoscale Al-rich and Pt-rich domains. The results of introducing such segregation into our model was striking, with the result being the generation of credible depictions of isotropic foamy sponges. It was helpful to increase the simulated volume to about a million atoms in order to properly visualize these structures, Figure 6.

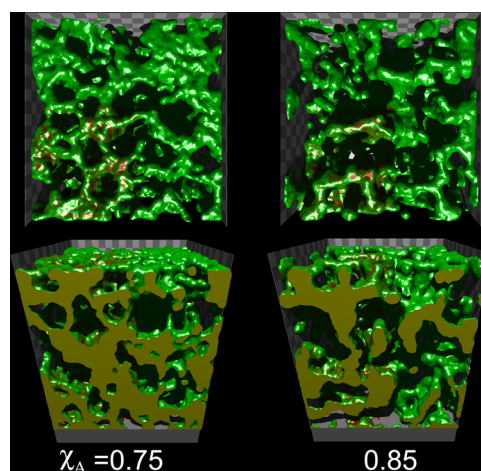


Figure 6. Sponges produced from an inhomogeneous starting structure of 950 000 atoms. The starting material consisted of spherical regions of $\chi_A = 1.0$ within a matrix of $\chi_A = 0.5$.

Films deposited at room temperature would also contain a high concentration of vacancies and defects,⁴⁵ factors that might, in principle, also influence the nature of the resultant sponges. A high vacancy concentration, for example, has been linked to more rapid de-alloying of AgMg.⁴⁶ Importantly, however, the morphology in that case remained fibrous. Similarly, a molecular dynamics simulation of the condensation of a random cloud of noble metal atoms also produced a fibrous sponge.⁴⁷ In support of this, our model also indicated that sponges produced from homogenous solid solutions remained fibrous *irrespective* of the vacancy concentration or stress state.

Further insight into the range of fibrous sponge morphologies possible from the model was gained by plotting $\langle M \rangle$ against $\langle G \rangle$ for precursors with systematically increasing χ_A , Figure 7. It is clear that there are some distinct transitions in morphology as χ_A is varied. There are two special morphologies, one with zero net mean curvature mean curvature (point B) and the other with zero net Gaussian

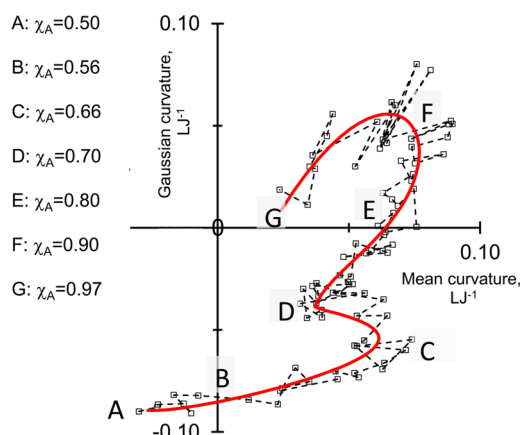


Figure 7. Evolution of sponges produced from homogeneous precursors at $t = 5000$ sweeps as χ_A is increased from 0.51 to 0.97. A–C are pin-hole sponges of gradually decreasing solid fraction, C–D are of a transitional nature between pin-hole and fibrous, D–F are classic bi-vermicular fibrous sponges, F–G represent morphologies in which percolation of the noble metal constituent becomes lost. E is a special sponge in which average Gaussian curvature is zero, that is, it has about as many saddle points as spherical protruberances or cavities.

curvature (point D). However, the former is correlated with a relatively low value of ν (~ 0.11), is of the pin-hole sponge type and is not completely de-alloyed. Sponge D, on the other hand, is the classic bi-continuous bi-vermicular morphology obtained by de-alloying homogenous precursors. Some applications, such as SERS, require a combination of percolation and the maximum positive mean curvature.⁴ Clearly sponges in the range D to E would be most suitable in that case.

Evidently, the microstructure of the precursor controls the sponge morphology on two scales. At the smallest scale it determines whether a fibrous or foamy sponge is formed. However, at a larger scale, a heterogeneous microstructure, for example a duplex arrangement of two phases of differing composition, will generate a bimodal distribution of pores in the sponge.^{6,8,17,22,48,49} If the phase with lower χ_A is continuous then its sponge can serve as a mechanical support for the less dense and more friable sponge formed by de-alloying the phase of higher χ_A . This is already practiced in the manufacture of some Raney nickel catalysts, the precursor of which may be formulated to contain a duplex mixture of NiAl (which is quite corrosion resistant) and Ni_2Al_3 (which is readily de-alloyed).¹⁹ Ideally, however, the phase of higher χ_A should itself be percolating so that it will produce an interconnected network of larger diameter channels within an already porous matrix.⁶

It has been mentioned earlier that negligible de-alloying occurs when χ_A of a bulk phase is less than about 0.5 or 0.6. Therefore, it is a legitimate question to ask how de-alloying of the sponge material can then actually proceed down to χ_A of as low as ~ 0.1 . Close examination of the dynamics of the Monte Carlo model provides a qualitative insight that is in agreement with the literature:⁵⁰ The Pt and Al are rapidly separated from one another within the narrow confines of a disorganized and vacancy-rich zone of the propagating de-alloying front. By the time the transformation front has passed, the remaining solid is already at its final χ_A of ~ 0.1 . However, once a solid phase with χ_{Al} below the parting limit has formed, little further de-alloying can occur. De-alloying is therefore a discontinuous, first-order, cellular transformation characterized by a well-defined front in

which considerable lateral movement ('surface diffusion') of the noble element occurs.

CONCLUSION

The morphology of nanoporous platinum sponges prepared by de-alloying thin-film precursors in aqueous alkali can be controlled by varying the composition and microstructure of the precursor. A sponge only forms when mole fraction of active element is greater than about 0.6, in both the experimental films and the simulations. There are systematic changes in morphology as χ_{Al} is increased, with sponges produced from crystalline precursors changing from a 'pin hole' type to 'fibrous' before becoming non-percolating at about $\chi_{\text{Al}} = 0.9$. Unusual isotropic foam sponges are obtained from metastable precursors deposited at room temperature. A hybrid cellular automaton/Metropolis Monte Carlo model was able to reproduce the range of morphologies observed experimentally and provided the basis for a quantitative examination of the progression of fibrous sponge morphologies as a function of χ_A .

ASSOCIATED CONTENT

Supporting Information

Additional electron microscope images of sponges. Graphs of average mean and Gaussian curvature as a function of precursor stoichiometry. This material is available free of charge via the Internet at <http://pubs.acs.org>.

AUTHOR INFORMATION

Corresponding Author

*Email : michael.cortie@uts.edu.au.

Notes

The authors declare no competing financial interest.

ACKNOWLEDGMENTS

A.P. and S.S. thank Nanosonics Limited of Australia and the Government of Thailand, respectively, for PhD support. The authors acknowledge the facilities and scientific and technical assistance of the Australian Microscopy & Microanalysis Research Facility at the University of Sydney and the Powder Diffraction beamline at the Australian Synchrotron, Victoria, Australia. We thank R. Wuhrer, M. Berkahn, J. Kimpton and C. Kealley for experimental assistance.

REFERENCES

- (1) Forty, A. J. Corrosion Micromorphology of Noble Metal Alloys and Depletion Gilding. *Nature* **1979**, *282*, 597–598.
- (2) Erlebacher, J.; Aziz, M. J.; Karma, A.; Dimitrov, N.; Sieradzki, K. Evolution of Nanoporosity in De-alloying. *Nature* **2001**, *410*, 450–435.
- (3) Crowson, D. A.; Farkas, D.; Corcoran, S. G. Geometric Relaxation of Nanoporous Metals: The Role of Surface Relaxation. *Scr. mater.* **2007**, *56*, 919–922.
- (4) Fujita, T.; Qian, L.-H.; Inoke, K.; Erlebacher, J.; Chen, M.-W. Three-Dimensional Morphology of Nanoporous Gold. *Appl. Phys. Lett.* **2008**, *92*, 251902.
- (5) Antoniou, A.; Bhattacharya, D.; Baldwin, K.; Goodwin, P.; Nastasi, M.; Picraux, T.; Misra, A. Controlled Nanoporous Pt Morphologies by Varying Deposition Parameters. *Appl. Phys. Lett.* **2009**, *95*, 073116.
- (6) Cortie, M. B.; Maaroo, A. I.; Stokes, N.; Mortari, A. Mesoporous Gold Sponge. *Aust. J. Chem.* **2007**, *60*, 524–527.
- (7) Cortie, M. B.; Maaroo, A.; Smith, G. B.; Ngoepe, P. Nanoscale Coatings of AuAl_x and PtAl_x and Their Mesoporous Elemental Derivatives. *Curr. Appl. Phys.* **2006**, *6*, 440–443.

- (8) Liu, W.; Zhang, S.; Li, N.; Zheng, J.; An, S.; Li, G. Influence of De-alloying Solution on the Microstructure of Monolithic Nanoporous Copper through Chemical De-alloying of Al 30 at. % Cu Alloy. *Int. J. Electrochem. Sci.* **2012**, *7*, 7993–8006.
- (9) Okman, O.; Kysar, J. W. Fabrication of Crack-Free Blanket Nanoporous Gold Thin Films by Galvanostatic De-alloying. *J. Alloys Compd.* **2011**, *509*, 6374–6381.
- (10) Li, H.; Misra, A.; Baldwin, J. K.; Picraux, S. T. Synthesis and Characterization of Nanoporous Pt–Ni Alloys. *Appl. Phys. Lett.* **2009**, *95*, 201902.
- (11) Pickering, H. W. Characteristic Features of Alloy Polarization Curves. *Corros. Sci.* **1983**, *23*, 1107–1120.
- (12) Wittstock, A.; Biener, J.; Erlebacher, J.; Bäumer, M. *Nanoporous Gold: From an Ancient Technology to a High-Tech Material*; Royal Society of Chemistry Publishing: Cambridge, 2012.
- (13) Ji, H.; Wang, X.; Zhao, C.; Zhang, C.; Xu, J.; Zhang, Z. Formation, Control and Functionalization of Nanoporous Silver through Changing De-alloying Media and Elemental Doping. *CrystEngComm* **2011**, *13*, 2617–2628.
- (14) Abburi, A.; Abrams, N.; Yeh, W. J. Synthesis of Nanoporous Platinum Thin Films and Application as Hydrogen Sensor. *J. Porous Mater.* **2012**, *19*, 543–549.
- (15) Chen, S.; Chu, Y.; Zheng, J.; Li, Z. Study on the Two De-alloying Modes in the Electrooxidation of Au–Sn Alloys by in Situ Raman Spectroscopy. *Electrochim. Acta* **2009**, *54*, 1102–1108.
- (16) Thorp, J. C.; Sieradzki, K.; Tang, L.; Crozier, P. A.; Picraux, S. T. Formation of Nanoporous Noble Metal Thin Films by Electrochemical De-alloying of Pt_xSi_{1-x}. *Appl. Phys. Lett.* **2006**, *88*, 033110.
- (17) Zhang, Q.; Zhang, Z. On the Electrochemical De-alloying of Al-Based Alloys in a NaCl Aqueous Solution. *Phys. Chem. Chem. Phys.* **2010**, *2010*, 1453–1472.
- (18) Sieradzki, K. Curvature Effects in Alloy Dissolution. *J. Electrochem. Soc.* **1993**, *140*, 2868–2872.
- (19) Smith, A. J.; Trimm, D. L. The Preparation of Skeletal Catalysts. *Annu. Rev. Mater. Res.* **2005**, *35*, 127–142.
- (20) Zhang, Z.; Wang, Y.; Wang, Y.; Wang, X.; Qi, Z.; Jia, H.; Zhao, C. Formation of Ultrafine Nanoporous Gold Related to Surface Diffusion of Gold Adatoms During De-alloying of Al₂Au in an Alkaline Solution. *Scr. Mater.* **2010**, *62*, 137–140.
- (21) Galinski, H.; Ryll, T.; Schlagenhauf, L.; Rechberger, F.; Ying, S.; Gauckler, L. J.; Mornaghini, F. C. F.; Ries, Y.; Spolenak, R.; Döbeli, M. De-alloying of Platinum–Aluminum Thin Films: Dynamics of Pattern Formation. *Phys. Rev. Lett.* **2011**, *107*, 225503.
- (22) Zhang, Z. H.; Wang, Y.; Qi, Z.; Zhang, W. H.; Qin, J. Y.; Frenzel, J. Generalized Fabrication of Nanoporous Metals (Au, Pd, Pt, Ag, and Cu) through Chemical De-alloying. *J. Phys. Chem. C* **2009**, *113*, 12629–12636.
- (23) McAlister, A. J.; Kahan, D. J. The Al–Pt (Aluminum–Platinum) System. *Bull. Alloy Phase Diagr.* **1986**, *7*, 47–51.
- (24) Feng, J.; Xiao, B.; Chen, J.; Dua, Y.; Yua, J.; Zhou, R. Stability, Thermal, and Mechanical Properties of Pt_xAl_y Compounds. *Mater. Des.* **2011**, *32*, 3231–3239.
- (25) Wu, K.; Jin, Z. Thermodynamic Assessment of the Al–Pt Binary System. *J. Phase Equilib.* **2000**, *21*, 221–226.
- (26) Kim, D. E.; Manga, V. R.; Prins, S. N.; Liu, Z.-K. First-Principles Calculations and Thermodynamic Modeling of the Al–Pt Binary System. *CALPHAD* **2011**, *35*, 20–29.
- (27) Piatti, G.; Pellegrini, G. The Structure of the Unidirectionally Solidified Al–Al₂₁Pt₃ Eutectic Alloys. *J. Mater. Sci.* **1980**, *15*, 2403–2407.
- (28) Wörle, M.; Krumeich, F.; Chatterji, T.; Kek, S.; Nesper, R. On the Structure and Twinning of PtAl₄. *J. Alloys Compd.* **2008**, *455*, 130–136.
- (29) Chattopadhyay, K.; Ramachandrarao, P. Metastable Phase Formation and Decomposition in a Rapidly Solidified Aluminium–Platinum Alloy. *Mater. Sci. Eng.* **1979**, *38*, 7–17.
- (30) Kovacs, A.; Barna, P. B.; Labar, J. L. The Nucleation and Growth of Intermetallic Al–Pt Phases in Co-Deposited Thin Films. *Thin Solid Films* **2003**, *433*, 78–81.
- (31) Murarka, S. P.; Blech, I. A.; Levinstein, H. J. Thin-film Interaction in Aluminum and Platinum. *J. Appl. Phys.* **1976**, *47*, 5175–5181.
- (32) Hurly, J.; Wedepohl, P. T. Optical Properties of Colored Platinum Intermetallic Compounds. *J. Mater. Sci.* **1993**, *28*, 5648–5653.
- (33) Tonejc, A. M.; A, T.; Bonefacic, A. Non-equilibrium Phases in Al-Rich Al–Pt Alloys. *J. Mater. Sci.* **1974**, *9*, 523–526.
- (34) Herrmann, A. K.; Formanek, P.; Borchardt, L.; Klose, M.; Giebler, L.; Eckert, J.; Kaskel, S.; Gaponik, N.; Eychemüller, A. Multimetallic Aerogels by Template-Free Self-Assembly of Au, Ag, Pt, and Pd Nanoparticles. *Chem. Mater.* **2014**, *26*, 1074–1083.
- (35) Fujita, T.; Chen, M. W. Characteristic Length Scale of Bicontinuous Nanoporous Structure by Fast Fourier Transform. *Jpn. J. Appl. Phys.* **2008**, *47*, 1161–1163.
- (36) Li, R.; Sieradzki, K. Ductile–Brittle Transition in Random Porous Au. *Phys. Rev. Lett.* **1992**, *68*, 1168–1172.
- (37) Biener, M. M.; Biener, J.; Wichmann, A.; Wittstock, A.; Baumann, T. F.; Bäumer, M.; Hamza, A. V. ALD Functionalized Nanoporous Gold: Thermal Stability, Mechanical Properties, and Catalytic Activity. *Nano Lett.* **2011**, *11*, 3085–3090.
- (38) Kucheyev, S. O.; Hayes, J. R.; Biener, J.; Huser, T.; Talley, C. E.; Hamza, A. V. Surface-Enhanced Raman Scattering on Nanoporous Au. *Appl. Phys. Lett.* **2006**, *89*, 053102.
- (39) Pickering, H. W.; Kim, Y. S. De-alloying at Elevated Temperatures and at 298 K—Similarities and Differences. *Corros. Sci.* **1982**, *22*, 621–635.
- (40) Lorenz, C. D.; May, R.; Ziff, R. M. Similarity of Percolation Thresholds on the Hcp and Fcc Lattices. *J. Stat. Phys.* **2000**, *98*, 961–970.
- (41) Ding, Y.; Kim, Y.-J.; Erlebacher, J. Nanoporous Gold Leaf: Ancient Technology/Advanced Material. *Adv. Mater.* **2004**, *16*, 1897–1900.
- (42) Chen, L.-Y.; Yu, J.-S.; Fujita, T.; Chen, M.-W. Nanoporous Copper with Tunable Nanoporosity for SERS Applications. *Adv. Funct. Mater.* **2009**, *19*, 1221–1226.
- (43) Erlebacher, J. An Atomistic Description of De-alloying—Porosity Evolution, the Critical Potential, and Rate-Limiting Behavior. *J. Electrochem. Soc.* **2004**, *151*, C614–C626.
- (44) Magnfält, D.; Abadias, G.; Sarakinos, K. Atom Insertion into Grain Boundaries and Stress Generation in Physically Vapor Deposited Films. *Appl. Phys. Lett.* **2013**, *103*, 051910.
- (45) Furrer, A.; Seita, M.; Spolenak, R. The Effects of Defects in Purple AuAl₂ Thin Films. *Acta Mater.* **2013**, *61*, 2874–2883.
- (46) Ji, H.; Zhang, C.; Xu, J.; Zhao, C.; Wang, X.; Zhang, Z. On the Vacancy-Controlled De-alloying of Rapidly Solidified Mg–Ag Alloys. *CrystEngComm* **2011**, *13*, 4846–4849.
- (47) Kolluri, K.; Demkowicz, M. J. Coarsening by Network Restructuring in Model Nanoporous Gold. *Acta Mater.* **2011**, *59*, 7645–7653.
- (48) Liu, W. B.; Zhang, S. C.; Li, N.; Zheng, J. W.; An, S. S.; Xing, X. L. A General De-alloying Strategy to Nanoporous Intermetallics, Nanoporous Metals with Bimodal, and Unimodal Pore Size Distributions. *Corros. Sci.* **2012**, *58*, 133–138.
- (49) Zhang, Z.; Wang, Y.; Qi, Z.; Somsen, C.; Wang, X.; Zhao, C. Fabrication and Characterization of Nanoporous Gold Composites through Chemical De-alloying of Two Phase Al–Au Alloys. *J. Mater. Chem.* **2009**, *19*, 6042–6050.
- (50) Szot, J.; Young, D. J.; Bourdillon, A.; Easterling, K. E. Cellular Morphologies in a De-alloying Residue. *Philos. Mag. Lett.* **1987**, *55*, 109–114.